Understanding the charge separation and transfer in mesoporous carbonate-doped phase-junction TiO$_2$ nanotubes for photocatalytic hydrogen production

Pengfei Wang[a], Qixing Zhou[a], Yuguo Xia[b], Sihui Zhan[a,*], Yi Li[c]

[a] MOE Key Laboratory of Pollution Processes and Environmental Criteria/Tianjin Key Laboratory of Environmental Remediation and Pollution Control, College of Environmental Science and Engineering, Nankai University, Tianjin 300350, China
[b] School of Chemistry & Chemical Engineering, National Engineering Research Center for Colloidal Materials, Shandong University, Jinan 250100, PR China
[c] Department of Chemistry, Tianjin University, Tianjin 300072, PR China

ARTICLE INFO

ABSTRACT

Novel mesoporous carbonate-doped phase-junction TiO$_2$ nanotubes were fabricated for the first time by a general simple and cost-effective strategy, namely, olive oil-assisted electrospinning. The as-prepared mesoporous carbonate-doped phase-junction TiO$_2$ nanotubes show a high photocatalytic hydrogen evolution activity of 6108 μmol h^{-1} g^{-1}, which is nearly six times higher than that of the commercially available P25. This outstanding photocatalytic performance originates from the morphology, electronic, crystal and textural structures of the photocatalysts. The refined porous structure can increase the optical path by multiple reflection effect, thus enhancing light harvesting. Particularly, first-principles calculations suggest that doping TiO$_2$ with carbonate can effectively reduce the bandgap of TiO$_2$, thus the absorbance of TiO$_2$ in visible light region can be highly enhanced. Moreover, anatase-rutile phase junctions were elaborately introduced into TiO$_2$ nanotubes by changing the anneal temperature and the roles of phase junctions are studied by photoelectrochemical measurements, which reveal that appropriate phase junction interface can significantly enhance the charge separation and transfer, hence achieving about 2 and 18 times photocurrent density enhancement compared to pristine anatase and rutile phase samples, respectively. Our study not only demonstrates a facile and eco-friendly strategy to synthesize highly efficient porous TiO$_2$-based nanotubes photocatalysts, but also provides a new strategy for rational design and synthesis of advanced photocatalysts by combining the strong synergistic effects of the morphology, electronic, crystal and textural structures.

1. Introduction

Photocatalytic hydrogen evolution (PHE) from water via semiconductor photocatalysts has been regarded as an efficient method to obtain the potential benefits of solar energy [1,2]. Although a lot of novel photocatalysts with various performances have been developed to data, titanium dioxide (TiO$_2$) remains of great interest as a model system because of its low cost, high chemical stability and the appropriate energies of the valence and conduction band, which are suitable for water oxidation and proton reduction, respectively [3,4]. Unfortunately, a low quantum yield, following its wide bandgap and the fast recombination of photoinduced electrons and holes, limits the use of TiO$_2$ for photocatalytic water splitting. And previous studies show that the photocatalytic activity of TiO$_2$ depends on its surface area, morphology, porosity, crystal phase and crystallinity [5]. In general, to

be high-performance photocatalysts, the TiO$_2$ particles must meet the following requirements: (i) high specific surface area; (ii) effective utilization of visible-light; (iii) efficient separation of photoinduced electrons and holes. Although these requirements have been studied individually, satisfying all of them simultaneously is challenging and has rarely been demonstrated before.

One dimensional (1D) porous nanofibers are of great interest in the fields of photocatalysis, owing to their high specific surface areas and effective paths for electron transportation [6]. Up to date, a series of methods have been used to fabricate mesoporous nanofibers, including hydrothermal [7], template-assisted process [8], electrospinning [6] and structure-selective synthesis [9]. Among them, the electrospinning technique has been rapidly developed in last decade for facile preparation of mesoporous fibers from submicron down to nanometer diameter, and few methods could match electrospinning in the field of

its flexibility, versatility and ease of fiber production. More importantly, further study shows that the fabrication of porous hollow nanofiber can further improve the specific surface areas. However, most of the reported works were focused on the fabrication of bare highly porous TiO_2 nanotubes for photocatalytic degradation of organics pollutants. Can we advance the porous TiO_2 nanotubes by introducing dopants in the electrospinning process? Such a breakthrough will lead to make TiO_2 photoactive in the visible region of the solar spectrum.

Until now, various dopants have been introduced into TiO_2, these include transition metal cations such as V, Cr, Fe, Ni, Sn, W and anions such as B, F, N, C, S [10–15]. Among them, carbon doping has been regarded as an efficient element, and recently, carbonate doping has received increasing attention and has been shown to extend the light absorption of TiO_2 from UV to visible region through effectively narrowing the TiO_2 bandgap [3,5,16]. In the doping process, some adventitious elemental carbon [5] or organic residues [17] would generate on the surface of TiO_2, and their effects on photocatalytic activity are not explored systematically. Moreover, we should pay more attention to phase-junction TiO_2 than pure phase TiO_2, and previous study has demonstrated that dual-phase TiO_2 photocatalysts with appropriate ratio of anatase to rutile have a higher photocatalytic activity as compared to either pure phase of anatase or rutile [18], because the composition identity on both sides of the interface in phase-junctions could give rise to continuous band bending, thus effectively enhance transfer across the interface and facilitate the carrier separation [19]. Unfortunately, the carbonate-doped anatase-rutile mixed TiO_2 and the effect on the photocatalytic hydrogen evolution have not been explored systematically to date.

In this work, we report an emulsion electrospinning method for preparing mesoporous carbonate-doped phase-junction TiO_2 nanotubes as a model system to explore how the photocatalytic activity is influenced by the morphology, carbonate-modification and phase-junction. In this method, the TiO_2 nanotubes form through the self-assembly of TiO_2 nanocrystals under electrospinning and calcination conditions. The morphology, carbonate-doping content and ratio of anatase to rutile can be varied by changing the initial titanium precursor composition and calcination temperature. The mesoporous nanotubes structure can effectively enhance lighttrapping and increase the specific surface area. DFT calculations indicate that doping TiO_2 with carbonate can effectively decrease the bandgap of anatase and rutile TiO_2. Photoelectrochemical tests indicate the separation of carries can be effectively improved by the dual-phase TiO_2. As a result, the mesoporous carbonate-doped phase-junction TiO_2 nanotubes exhibit strong photocatalytic activity, and the photocatalytic hydrogen evolution rate can be $6108\,\mu mol\,h^{-1}\,g^{-1}$, which is significantly higher than those from various other TiO_2 photocatalysts. The well-defined morphology, visible light absorption and photoinduced electron/hole separation make the mesoporous carbonate-doped phase-junction TiO_2 nanotubes excellent candidates for applications in solar energy conversion.

2. Experimental

2.1. Fabrication of mesoporous carbonate-doped phase-junction TiO_2 nanotubes

Mesoporous carbonate-doped phase-junction TiO_2 nanotubes were prepared by calcination of precursor fibers, which were obtained by electrospinning the solution of polyvinylpyrrolidone (PVP), titanium butoxide (TBOT) and olive oil. The raw materials of TBOT (Aladdin, Shanghai, China), PVP (MW ≈ 1300000, Energy Chemical, Shanghai, China) and olive oil (Borges, Beijing, China) were purchased and used directly without further purification. Anhydrous ethanol and glacial acetic acid were used as the solvents to uniformly mix TBOT, PVP and olive oil. Typically, 4.5 g TBOT was dissolved in 5.25 g anhydrous ethanol and 7.75 g glacial acetic acid with stirring for 1 h. Then 1.75 g PVP and 4.5 g anhydrous ethanol were added into the above solution

slowly and stirred vigorously for 2 h to form a viscous gel of PVP/titanium acetate complex solution. Next, 5.25 g olive oil was added to the complex solution and stirred continuously for 2 h to form a stable and homogeneous emulsion. As for a typical electrospinning process, the obtained solution was transferred into a plastic syringe with a spinneret (anode, diameter 0.6 mm). The typical distance between the spinneret and the collector (cathode) was about 12 cm. A direct current voltage of 17 kV was applied for electrospinning the precursor fibers, and the environmental temperature was maintained at 60 °C during the electrospinning process. After electrospinning, the collected non-woven nanofibers were dried in oven at 80 °C overnight. Finally, the as-spun nanofibers were positioned in a crucible and calcined in a muffle furnace at 350 °C, 400 °C, 450 °C, 550 °C, 650 °C, 750 °C for 4 h, before cooling to the ambient temperature. And the products were labeled as CT (Carbonate-doped TiO_2 nanotube)-350, CT-400, CT-450, CT-550, CT-650, CT-750, respectively. To evidence the universal applicability of this technique for producing mesoporous nanotubes, TiO_2-based hybrid mesoporous nanotubes were also fabricated with the similar method. Copper acetate ($Cu(Ac_2)$) and Nickel acetate ($Ni(Ac_2)$) were used as the raw materials in the synthesis of TiO_2/CuO and TiO_2/NiO hybrid nanotubes, respectively. The particular compositions of the initial solutions are shown in Table S1 (SI), and the resultant nanotubes were labeled as TCu and TNi, respectively.

For comparison, control experiments were also carried out without electrospinning process and olive oil addition, respectively. And they were labeled as CP-450 and CF-450, which represented Carbonate-doped TiO_2 nanoparticles and Carbonate-doped TiO_2 nanofibers, respectively.

2.2. Characterization

The morphology of the prepared samples was observed by the field-emission scanning electron microscopy (FESEM, Hitachi SU8010 at an accelerating voltage of 3 kV, Japan). The microstructure of the samples was further analyzed using transmission electron microscopy (TEM, a JEOL JEM-2100F at an accelerating voltage of 200 kV, Japan). The Rigaku D/Max 2200PC X-ray diffractometer (XRD) with Cu Kα radiation (λ = 0.15418 nm) was used to obtain the crystalline structure of the samples. The Micromeritics ASAP 2460 system was used to determine the Brunauer-Emmett-Teller (BET) specific surface areas the samples at liquid nitrogen temperature. The samples were degassed at 180 °C for 5 h prior to BET measurements. The pore size distributions were estimated by the Barret-Joyner-Halenda (BJH) method. The thermal behaviors were analyzed by a TG209 thermogravimetric analyzer (NETZSCH, Germany). The Bruker RFS 100/S Raman microscope with excitation laser beam wavelength of 1064 nm was used to obtain the Raman spectra of the samples. The Thermal ESCALAB 250 electron spectrometer using Al Kα radiation X-ray source (hν = 1486.6 eV) was used to determine the valence states of all elements via X-ray photoelectron spectroscopy (XPS). The Shimadzu Corporation UV–vis spectrophotometer was used to record the absorption spectra of the samples. The Thermo Nicolet iS5 FTIR spectrometer equipped with a liquid-nitrogen-cooled MCT detector was used to record the Fourier transform infrared spectra (FTIR) of the samples. The Bruker model A300 EPR spectrometer with microwave power of 1 mW was used to record the electron paramagnetic resonance (EPR) spectra. In each measurement, 20 mg of sample was place in a quartz EPR tube and measured at 100 K. The Edinburgh Instruments FLS920P equipped with a Xe lamp-920 at room temperature was used to measure the photoluminescence (PL) spectra of the photocatalysts.

2.3. Photocatalytic hydrogen evolution test

The photocatalytic hydrogen evolution test was carried out in a test installation. The photo reactor was a quartz flask of 150 mL and a full spectrum solar simulator (CEL-S500) with AM 1.5G filter was used as

the light source, which was about 1 Sun power. In a typical photocatalytic experiment, 100 mg of photocatalyst powder was suspended in 100 mL aqueous solution containing 10 vol.% triethanolamine (TEOA) as sacrificial electron donor. 1.0 wt.% of Pt was loaded on the surface of photocatalyst by the in-situ photodeposition approach using H_2PtCl_6. Then the reaction system was thoroughly degassed by evacuation. Next, the mixture was illuminated under continuous magnetic stirring and a water-cooling filter was used to keep the reaction temperature at ca. 10 °C. The generated gas spread into the quantitative loop (1 mL) of a six-way valve, and the gas volume was analyzed by gas chromatography equipped with a thermal conductive detector every 60 min to determine the hydrogen generation rate.

The apparent quantum efficiency (QE) at a wavelength of 365 nm, 420 nm, 475 nm and 520 nm was measured under the identical reaction condition by placing various band-pass filters in front of the light source. The CEL-NP2000 spectroradiometer was used to measure the intensity of the incident light. The apparent QE was calculated according to the following equation:

$$
\begin{aligned}
AQE &= \frac{number\ of\ reacted\ electrons}{number\ of\ incident\ photons} \times 100\% \\
&= \frac{number\ of\ evolved\ H_2\ molecules \times 2}{number\ of\ incident\ photons} \times 100\%
\end{aligned}
$$

2.4. Photoelectrochemical measurements

The photoanodes were fabricated as follows: 4 mg sample, 1 mL ethanol and 20 μL nafion were mixed by sonication for 30 min to make a slurry. The slurry was then dropped onto an indium-tin oxide (ITO) glass. After the ethanol evaporated thoroughly at ambient temperature, the photoanodes were dried at 60°C for 8 h. The areas of the photoanodes are 2.75 cm^2. Photoelectrochemical (PEC) performances of the prepared photoanodes were recorded on an electrochemical work station (CHI660E Instruments) with a standard three-electrode system (an Ag/AgCl electrode reference electrode and a Pt foil counter electrode). 0.5 M $NaSO_4$ solution was used as the electrolyte. The measured potential vs. Ag/AgCl was converted to reversible hydrogen electrode (RHE) scale using the Nernst equation: $E_{RHE} = E_{Ag/AgCl} + 0.197 + 0.059\ pH$. A 300 W Xe lamp was used as a light source. Typically, J-V curves were recorded at a scan rate of 5 mV s^{-1} and the chopped illumination was used to examine transient photocurrents. Transient photocurrent measurements with chopped illumination were also conducted to examine the steady-state photocurrent densities of the photoanodes. Electrochemical impedance spectra (EIS) were carried out in the frequency range of 0.05–10^5 Hz.

The incident photon-to-current efficiency (IPCE) was measured at 1.0 V vs. RHE. A 300 W Xenon lamp coupled with various band-pass filters in front of the reactor was used to generate a monochromatic beam. The incident light intensity was measured using a spectroradiometer. IPCE under each wavelength was determined by the following equation:

$$
IPCE(\lambda) = \frac{1240I}{\lambda J_{light}}
$$

where λ is the wavelength of incident beam, I is the photocurrent density at each specific wavelength and J_{light} is the irradiance at each specific wavelength.

2.5. Computational details

The density functional theory calculations corrected by on-site Coulomb interaction have been performed by using the Vienna Ab-initio Simulation package to investigate the electronic structure of C-doped anatase and rutile TiO$_2$. Supercell models involving 48 atoms were constructed with periodically $(2 \times 2 \times 1)$ and $(2 \times 2 \times 2)$ for anatase and rutile TiO$_2$, respectively, and structure of C-doped TiO$_2$

were modeled by replacing one Ti atom with one C atom [20]. The cell parameters of pristine anatase and rutile TiO$_2$ were optimized by performing spin-polarized Perdew-Burke-Ernzerhof (PBE) exchange-correlation functional within the generalized gradient approximation (GGA), while atomic positions of the supercell and C-doped structure as well as corresponding electronic structure were calculated by GGA + U calculations with a Hubbard parameter U (4.2 eV) introduced to account for the strong on-site Coulomb repulsion among the localized Ti-3d electrons. The wave functions were expanded in a plane wave basis with an energy cutoff of 500 eV, using the projector augmented wave (PAW) method. The Brillouin-zone integration was performed using a $4 \times 4 \times 3$ and $3 \times 3 \times 5$ Monkhorst-Pack grid for supercell structure of anatase and rutile TiO$_2$. For all the calculations, spin polarization was taken into account and the convergence criteria for the electronic and ionic relaxation are 10^{-5} eV and 0.02 eV/Å, respectively.

3. Results and discussion

3.1. Effect of the morphology on photocatalytic activity

First of all, scanning electron microscopy (SEM) was employed to observe the morphology of the as-spun nanofibers and their corresponding calcined products. The as-spun nanofibers of CF samples have smooth surfaces, and the diameter is consistently about 800 nm, with a length of several hundred of millimeters (Fig. S1a and b). For the as-spun CT samples, the formation of hollow structures can be observed distinctly, and the diameter is about 4 μm, which is ascribed to the exist of olive oil (Fig. S1c and d) [21]. Figs. S2 and S3 show uniform spatial distribution elemental mapping of C, N, O and Ti of as-spun CF and CT samples, indicating that TBOT, PVP, olive oil had been mixed uniformly. Fig. 1a shows the representative morphology of mesoporous nanotubes by CT-450 (also see Fig. S4a–c), indicating the as-spun nanofibers have been converted into mesoporous nanotubes completely. As can be seen from Fig. 1b, there are many pores on the surface of the nanotubes. Pores with an approximate diameter of 30 nm are distributed evenly on the surface of the nanotubes.

A typical TEM image of a single CT-450 nanotube is shown in Fig. 1c. The SAED pattern of the marked area (red circle) indicates that the obtained nanotubes are anatase and rutile mixed TiO$_2$ (JCPDS, No. 00-021-1272 and No. 00-021-1276) with a polycrystalline nature. The HRTEM (Fig. S4d-f) shows the mixed crystalline anatase phase and rutile phase particles of different sizes. The fringes of spacing 0.353 and 0.329 nm correspond to (101) plane of anatase TiO$_2$ and (110) plane of rutile TiO$_2$, respectively. HRTEM gave direct evidence of the distribution of anatase and rutile particles. Furthermore, the element mappings disclose that the nanotubes possess Ti, O and C (Fig. 1g-i), indicating that there is small amount of carbon species in the calcined nanotubes, which come from olive oil. And the photocatalytic activity will be enhanced by carbon species, which will be discussed later. Fig. 1d shows the typical XRD pattern of CT-450 samples. There are typical anatase and rutile TiO$_2$ peaks, suggesting the mix phase of the resultant products. And the highly crystalline of the samples can be confirmed by the sharp diffraction peaks.

A surface analysis using N$_2$ adsorption-desorption isotherm (Fig. 1e) reveals that the nanotubes show type IV isotherm curve with obvious H3-type hysteresis, implying that the as-synthesized nanotubes are mesoporous with a Brenauer-Emmett-Teller (BET) surface area of ~48.95 m^2/g [6]. The Barrett-Joyner-Hanlenda (BJH) analysis from the desorption branches (Fig. 1f) further affirms the mesoporous nature of the nanotubes since it shows a narrow pore size distribution of about ~10 nm.

The control experiments without electrospinning and without olive oil added in the initial solutions were carried out to isolate the effects of electrospinning technology and the olive oil on the formation of the mesoporous nanotubes, respectively. The CP-450 samples through direct thermal decomposition of precursor show the morphology of bulk
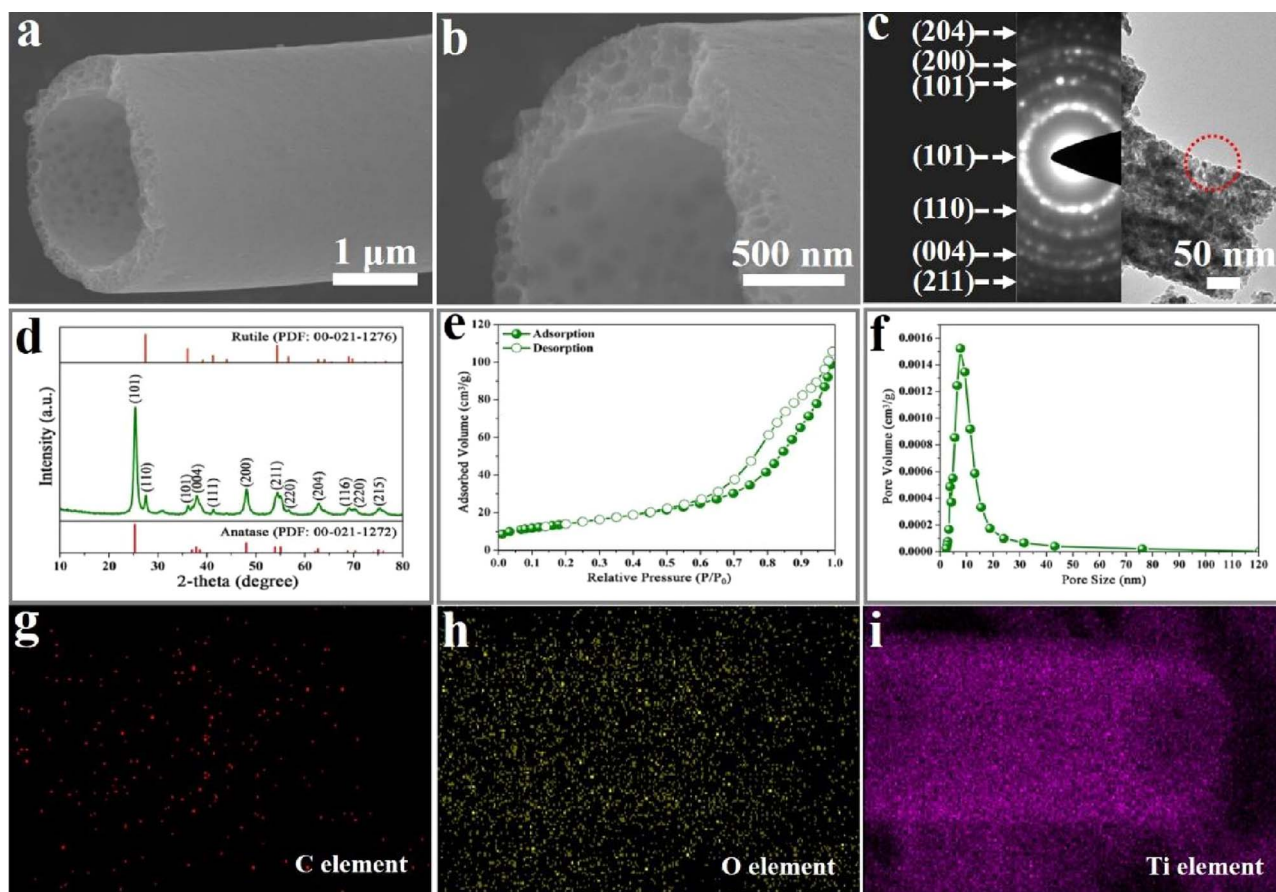
Fig. 1. (a, b) Typical SEM images of CT-450 under different magnifications. (c) A representative TEM image of a single CT-450 mesoporous nanotube. The inset is the corresponding SAED pattern recorded from the marked area in panel c. (d) A typical XRD pattern of CT-450 after calcination. (e) Nitrogen adsorption-desorption isotherm of CT-450. (f) Corresponding pore size distribution of CT-450. (g-i) The element mappings of C, O and Ti within a single CT450 nanotube.

(Fig. S5a–b), and they show the BET surface area of ca. 8 m^2/g, which is about 6 times lower than that of CT-450 samples. For CF-450 samples (Fig. S5c–d), the products present the conventional solid nanofibers, which are quite different from the CT-450 samples synthesized with olive oil, suggesting that the introduced olive oil has a critical effect for the formation of the mesoporous nanotubes. The XRD pattern (Fig. S5e) indicates that the as-prepared CF-450 sample is also mixed phase of TiO$_2$, implying that the olive oil has no effect on the crystalline phase. Whereas the BET surface area of the CF-450 sample is only about 12.6 m^2/g (Fig. S5f), which shows 4 times lower than that of CT-450 sample. As a result, the comparison clearly suggests (i) the effect of olive oil on the formation of the mesoporous nanotubes is crucial, which helps create the pores and hollow structure and (2) the olive oil plays a vital role on enhancing the BET surface area of the nanotubes. Based on the above analysis, the proposed mechanism of formation of the mesoporous nanotubes could be proposed as follows (Fig. S6–S7). Furthermore, we have proved the catholicity of the olive oil-assisted electrospinning technique for fabricating mesoporous TiO$_2$-based nanotubes (Figs. S8–S10).

The as-fabricated CP-450, CF-450 and CT-450 samples, as well as the commercial P25, were used as the photocatalysts to confirm the effect of the morphology on photocatalytic activities. And the photocatalytic activity of all samples was evaluated by hydrogen production from water under simulated solar light using Pt as cocatalyst and triethanolamine as hole scavenger. As shown in Fig. 2a, CT-450 indeed much enhances the activity, and a peak hydrogen production rate of 6108 μmol h^{-1} g^{-1} is achieved, which is nearly six times higher than that of P25. Interestingly, CP-450 also shows higher activity than P25, and this can be ascribed to the exist of carbon species, which can

narrow the bandgap and enhance electron-hole pairs separation, and this will be discussed later [22]. This character can be confirmed by the electrochemical impedance spectroscopy (EIS) (Fig. 2b), CP-450 has a smaller arc radius than that of P25, suggesting the charge transfer resistance of CP-450 is decreased by the carbon species in CP-450 [19]. It is well known that, the one-dimensional (1D) structure could remarkably inhibit the agglomeration of nanoparticles and has effective paths for electron transportation, which contributes to the stable photocatalytic performance [23]. And it is the reason why CF-450 and CT-450 have enhanced photocatalytic performance than CP-450. Furthermore, the mesoporous architecture plays a key role in photocatalytic hydrogen production. When the porous surfaces are irradiated by light, the photons will enter the pore canals. For the photons, some of them are absorbed directly for photocatalysis, and some are reflected. It is with the pores that a majority of the reflected photons remain within the pores until completely absorbed, implying that the photon application efficiency can be effectively improved by the porosity. Furthermore, the larger specific surface and the columnar hollow mesoporous architecture of CT-450 can offer more active sites to adsorb reactants, which can enhance the reaction with water and TEOA. In a word, this should be a result of the synergy of the enhanced light absorption, larger specific surface and improve carrier transfer and separation, which will be discussed systematically later. And we also can summarize that the morphology of the 1D hollow mesoporous nanotubes is beneficial to the photocatalytic hydrogen production.

3.2. Crystal structure and chemical states

As mentioned above, the morphology of CT-450 plays a great role in
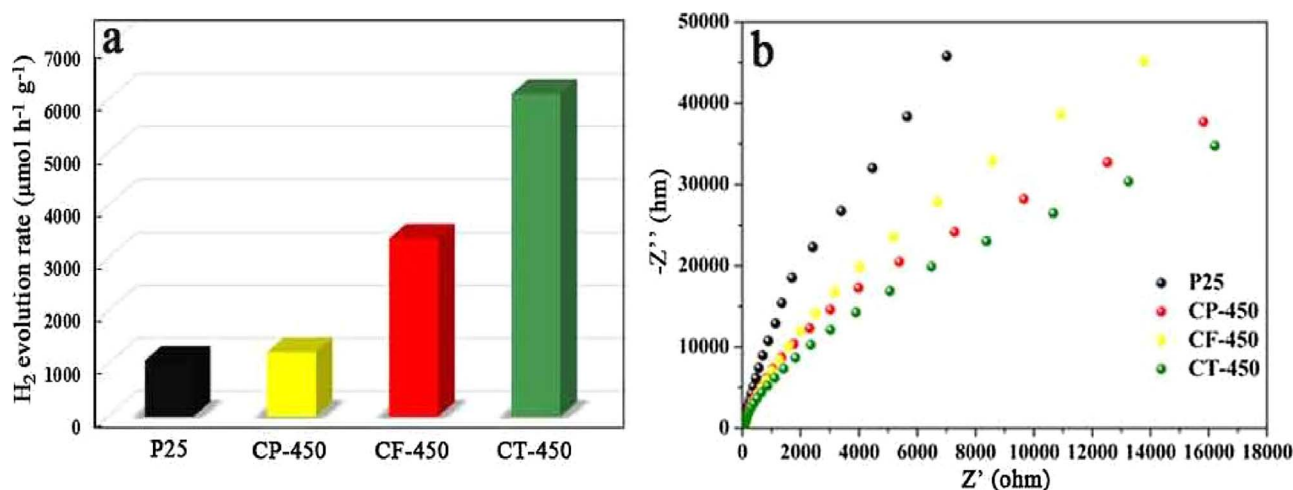
Fig. 2. (a) Photocatalytic hydrogen production rate for P25, CP-450, CF-450 and CT-450 samples under simulated solar light. (b) Electrochemical impedance spectroscopy for P25, CP-450, CF-450 and CT-450 samples under dark condition.
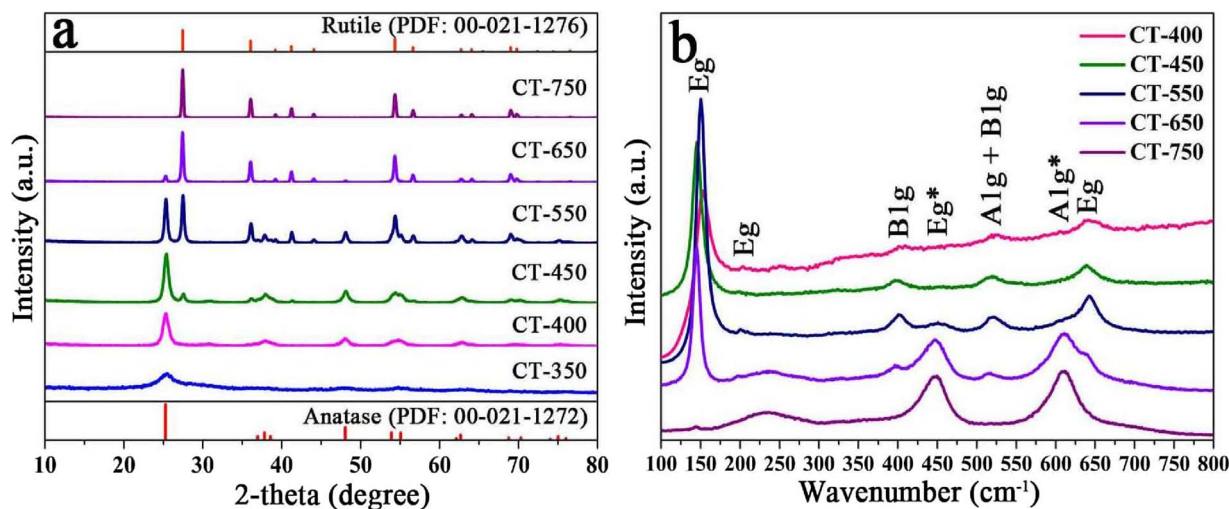

Fig. 3. XRD and Raman patterns show the transition from pure anatase to anatase-rutile phase-mixtures to pure rutile with an increasing in temperature.

Table 1
Physical properties of the CT samples.

sample	phase composition (%), [A:R]		bandgap (eV)	crystal size (nm)	S_{BET} (m²g⁻¹)	PV (cm⁻³g⁻¹)
	XRD	Raman				
CT-400	100:0	100:0	2.54	9	75.25	0.19
CT-450	85:15	84:16	2.75	17.4	48.95	0.16
CT-550	44:56	47:53	2.80	19.6	25.56	0.12
CT-650	10:90	18:82	2.80	29.8	10.94	0.055
CT-750	0:100	0:100	2.85	51.7	5.95	0.03

photocatalytic hydrogen production. However, the underlying cause of this improvement is not fully understood. Thus, a series of CT materials were obtained by changing the calcination temperature to understand the role of homo-junctions and carbon species in photocatalytic hydrogen production. XRD patterns in Fig. 3a display the crystal phase evolution of CT samples prepared with different calcination temperature. For CT-350, no evidence of good crystalline phase can be observed, although the samples were subjected to continuous calcination at 350 °C for 4 h [24]. Upon calcination in air at 400 °C, CT samples were formed in the predominant content of pure anatase.

The anatase to rutile phase transformation typically occurs above

400 °C, and the samples annealed at 450, 550 and 650 °C showed varying amounts of the two phases. When the samples were annealed at 750 °C for 4 h, only the rutile phase was observed. The refined scale phase fraction can be estimated from integrated intensities of anatase (101) and rutile (110) peaks, using the following equations

$$W_a = \frac{K_a A_a}{(K_a A_a + A_r)} \tag{1}$$

$$W_r = \frac{A_r}{(K_a A_a + A_r)} \tag{2}$$

where W_a and W_r are the mass fractions of anatase and rutile, respectively. A_a and A_r are the integrated intensities for each polymorph correspondingly. K_a is the correction coefficient, which the value is 0.886 [18]. It is noteworthy that the mass fraction of anatase in CT-450 was 85%, which is similar to that in P25. The phase fractions of the samples obtained under different calcination temperatures are shown in Table 1 and lattice parameters list in Fig. 4f. In order to further investigate the crystalline phase, Raman spectra have been measured and shown in Fig. 3b. The stacked Raman spectra show the transition from pure anatase to anatase-rutile phase-mixtures to pure rutile with an increase in temperature. Non-asterisked and asterisked symmetries refer to anatase and rutile respectively. Fig. S11 shows the deconvolution of the A1g (~639 cm⁻¹) and Eg (~612 cm⁻¹) bands of anatase and rutile respectively. As can be seen from Table 1, the phase
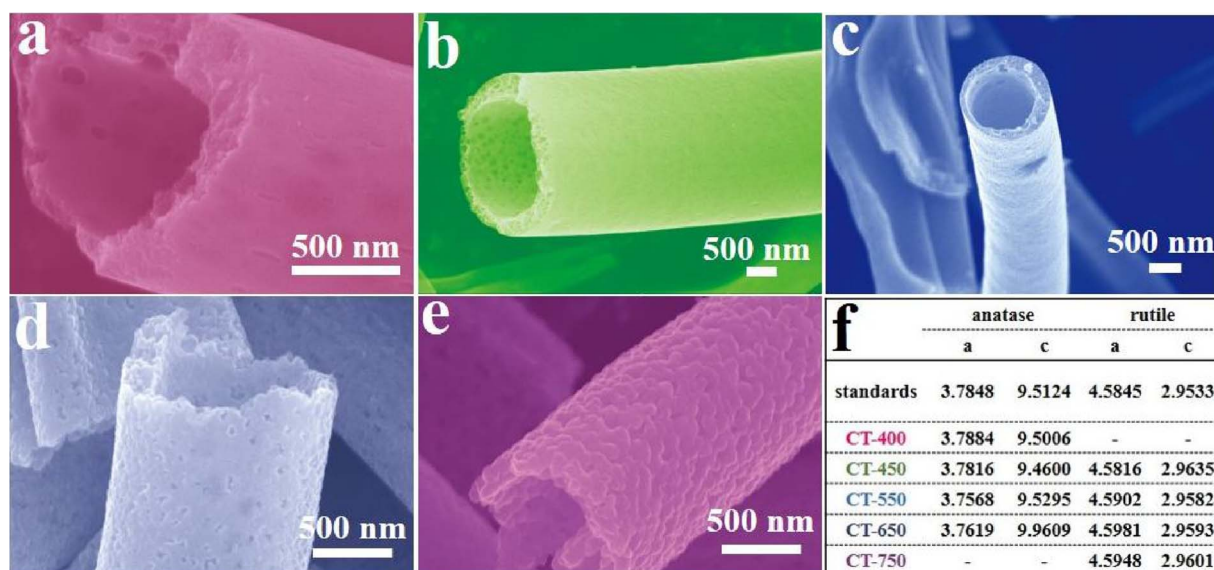
	anatase		rutile	
	a	c	a	c
standards	3.7848	9.5124	4.5845	2.9533
CT-400	3.7884	9.5006	-	-
CT-450	3.7816	9.4600	4.5816	2.9635
CT-550	3.7568	9.5295	4.5902	2.9582
CT-650	3.7619	9.9609	4.5981	2.9593
CT-750	-	-	4.5948	2.9601

Fig. 4. SEM images of as-spun composite nanofibers after calcination at various temperatures of (a) 400, (b) 450, (c) 550, (d) 650 and (e) 750 °C for 4 h. (f) Unit cell lattice parameters derived from XRD data.

compositions of the samples obtained from Raman are good consistent with XRD. And the phase fractions determined by XRD and Raman are plotted in Fig. S12, which clearly show the phase transformation with the temperature increasing.

Fig. 4 illustrates the SEM images which clarified the microstructure of the CT samples after calcination at various temperatures. While no significant effect of temperature on the surface morphology was observed in the report by Wu on TiO_2 nanorods [25], in this work, the SEM images vividly illustrate that as the calcinations temperature increases, the surface of the CT samples have evolved from a smooth porous surface structure (Fig. 4a–c), into a rough non-porous surface (Fig. 4d–e), and the pores become bigger and bigger. Higher temperature could promote fusion and growth of the granular nanocrystals into larger crystals [26] thus possibly resulting in a rough surface structure (Table 1). The higher the calcination temperature, the greater the shrinkage, because of the degradation of PVP and olive oil contents. Nevertheless, the overall morphology remained hollow nanotubes of the calcinations temperature. And the unit cell of either phase did not expand by more than 1% relative to a powder standard with increased temperatures (Fig. 4f).

Bueno-Ferrer et al. [27] reported that larger crystals exhibit lower specific surface area. Likewise, in this study, CT-750 had the least specific surface area as well-corroborated by the measured BET specific surface area as depicted in Table 1. Both CT-400 and CT-450 have the relatively high specific surface area, implying enhanced adsorption capability for mass transfer. Meanwhile, the N_2 adsorption-desorption isotherm (Fig. 5a) technique shows that CT-400, CT-450, CT-550 and CT-650 are mesoporous structure, however, CT-750 is not mesoporous, which is in good agreement with the rough surface morphology as shown in Fig. 4. The disappearance of mesoporosity is ascribed to the grown of crystals which has diminished the pores. Fig. 5b shows the pore size distributions of CT samples calcined at different temperature. The pore size has been larger and larger with the temperature increased to 650 °C, and the unusual plot of CT750 further corroborated the absence of mesoporosity due to the enhanced crystal growth at higher calcinations temperature. The high specific surface area and mesoporous structures play important role in photocatalytic reaction, which will be discussed later.

As mentioned above, the carbon species in CT samples also play a key role in photocatalytic reactions, thus to investigate the forms and the chemical states of the carbon species, X-ray photoelectron spectroscopy (XPS) was applied to record the C 1s, Ti 2p and O 1s XPS

spectra of P25, CT-400, CT-450 and CT-750, as shown in Fig. 6. Fig. 6a–c shows the C 1s spectra of CT-400, CT-450 and CT-750 from 280 to 294 eV, respectively. Indeed, the C 1 s XPS spectra show carbon-containing adsorbents, which come from the combustion of the olive oil. The carbon-containing products of olive oil can adsorb on TiO_2 nanocrystal surface and some may be trapped in growing TiO_2 tetrahedra during the anneal process, which incorporates carbon into TiO_2. The C 1s peak at ∼284.7 eV arises from the C−C neutral bond and might overlap with the graphite-like C−C bonding (285.0 eV), whose large intensity is an pointer of carbonate species doped into TiO_2[28]. And the intensity of C−C peak decreases gradually as the calcination temperature increasing (Fig. S13), indicating there are more graphite-like carbon in CT-400. Furthermore, the peaks centered at 286.0 (CT-400, CT-450 and CT-750) and 288.8 eV (CT-450) are similar to the oxidized carbon species such as C−OR(H), C=O, or C−OOR(H) that might be associated with the formation of carbonate-like species due to interstitial carbon in the TiO_2 lattice[5], indicating all the three samples were doped by carbonates successfully. However, the expected Ti−C bonds centered at ∼282 eV are absent in the XPS spectra, indicating the oxygen species in the TiO_2 lattice do not be substituted by the carbon species [29]. The high resolution XPS spectra of Ti 2p regions are shown in Fig. 6d. For P25, the two main characteristic peaks of Ti 2p core-level of TiO_2, corresponding to the Ti $2p_{3/2}$ (458.7 eV) and Ti $2p_{1/2}$ (464.4 eV), respectively, which indicates the presence of Ti^{4+} ions [28]. For CT-400, the intensities of the two peaks decrease and shift to higher binding energies at 458.9 and 464.6 eV, respectively, which are resulted from the excess carbon species uniformly covered TiO_2 nanocrystal surface rather than substitute into the crystal lattice[30]. For CT-450, the similar Ti 2p peaks at 458.7 and 464.4 with P25 suggest that the carbon species reduced with the temperature increased. However, for CT-750, the Ti $2p_{3/2}$ and Ti $2p_{1/2}$ peaks negatively shifted to 458.5 and 463 eV, respectively. This suggests non-stoichiometric TiO_2 (i.e. oxygen vacancies) might be formed in CT-750[22], caused by the decomposition of olive oil, which will be discussed later. The XPS spectra of O 1s (Fig. 6e) of CT-400, CT-450 and CT-750 samples show a well-developed peak at ∼530 eV, and a hump is observed at higher biding energy of ∼531 eV. The peak at ∼530 eV is attributed to the lattice oxygen of TiO_2 while the peak at 531.6 eV is associated with C−O and C=O bonds in carbonate groups [5]. Fig. 6f shows the valence band (VB) XPS of CT-400, CT-450 and CT-750 samples. For the VB-XPS of CT-400, CT-450 and CT-750, the main absorption onsets are located 0.83, 1.15 and 1.30 eV, respectively, and their VB tops take maximum
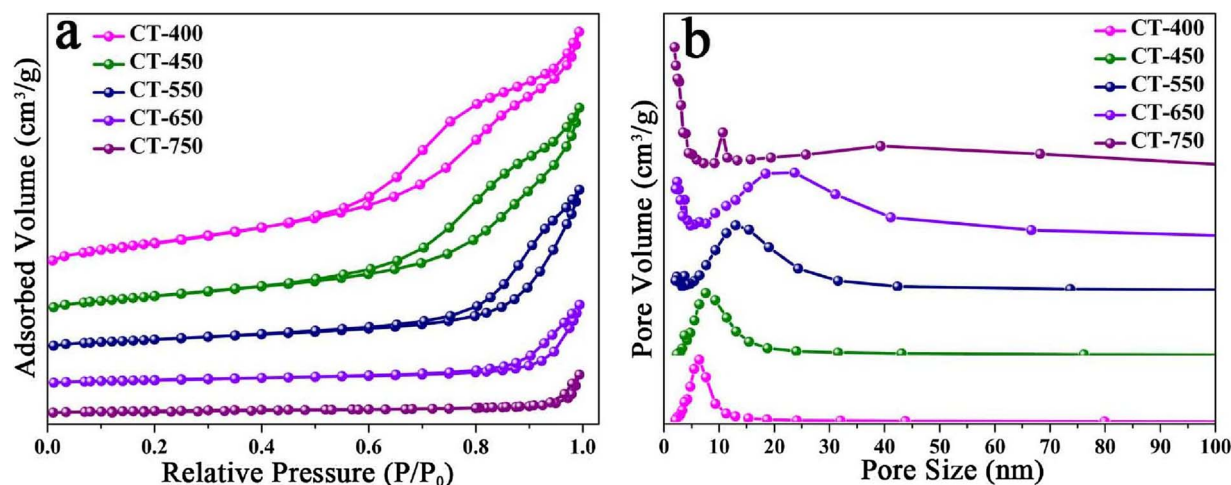
Fig. 5. (a) N_2 adsorption/desorption isotherm curve and (b) BJH pore size distributions of CT composite calcined at different temperatures.
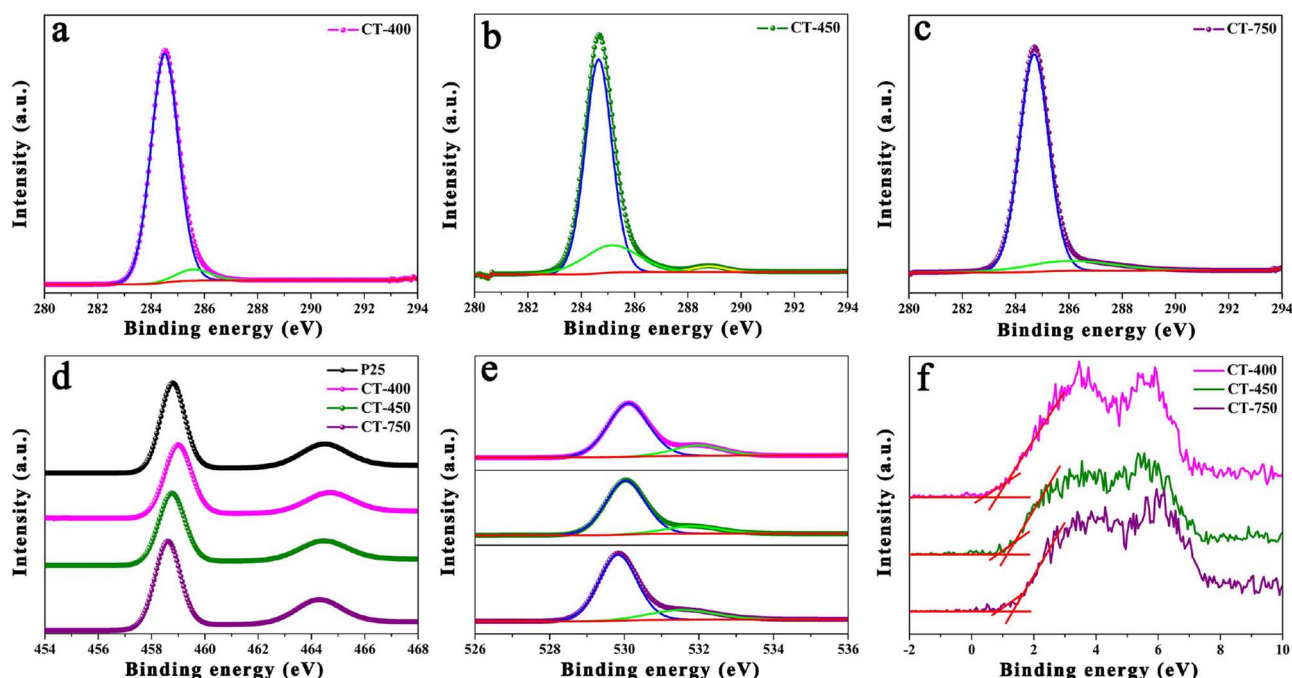

Fig. 6. XPS spectra for (a–c) C 1s, (d) Ti 2p, (e) O 1s and (f) VB XPS of the samples.

blue shift toward the vacuum level at approximately 0.34, 0.78 and 0.81 eV compared with reference TiO_2 [22]. The notable difference compared with the reference TiO_2 is the presence of a band tail induced by structural disorders, which come from the presence of carbonates, leading to enhanced visible light adsorption [31].

3.3. Optical properties and electronic structure

The diffuse reflectance UV–vis spectra were used to clarify the strengthen absorption of visible light by carbonate-doped CT samples, and we chose Degussa P25 as a reference material. As can be seen from Fig. 7a, it is found that the CT samples exhibit stronger absorption than P25 over all the regions, remarkably in the visible region. The enhanced light absorption of CT samples is mainly attributed to the doping with carbonate-like and graphite-like carbon species, which can be confirmed from the color of the samples. The color of CT-350 is dark (inset in Fig. 7a), and this is ascribed to the carbonization of the olive oil and organics. For the other CT samples, the colors are grey, and the color depth depends the calcination temperature, indicating the decrease of

carbon species. And this also can be confirmed by the FT-IR spectra (Fig. S14). For CT-400, it has the strongest peaks than the other CT samples, which indicated that the organics have not been decomposed. However, for the other CT samples, the peaks have been decreased with the increased temperature, indicating the decomposition of the carbon species. We further calculated the band gap and position of the CT samples from the Tauc plot (Fig. 7b) obtained from UV-DRS results [32]. The obtained band gap values are 2.95, 2.69, 2.74, 2.86 and 2.91 eV for CT-400, CT-450, CT-550, CT-650 and CT-750, respectively. The bandgaps of the CT samples are narrower than P25 (3.16 eV) [18], which could be ascribed to the carbonate doping in the TiO_2 bandgap. Therefore, these results are consistent with the DFT calculations. CT-450 has the narrowest bandgap, indicating the optimal doping amount. However, with increasing the temperature the bandgaps of the samples increase correspondingly, which could be ascribed to the reduction of carbon species. Thus, the absorbance in the visible light region of CT-450 has been highly enhanced, and the absorption band edge moves to longer wavelengths (Fig. S15). It can also be seen from Fig. 7a, CT-550, CT-650 and CT-750 show higher light absorption than CT-400 and CT-
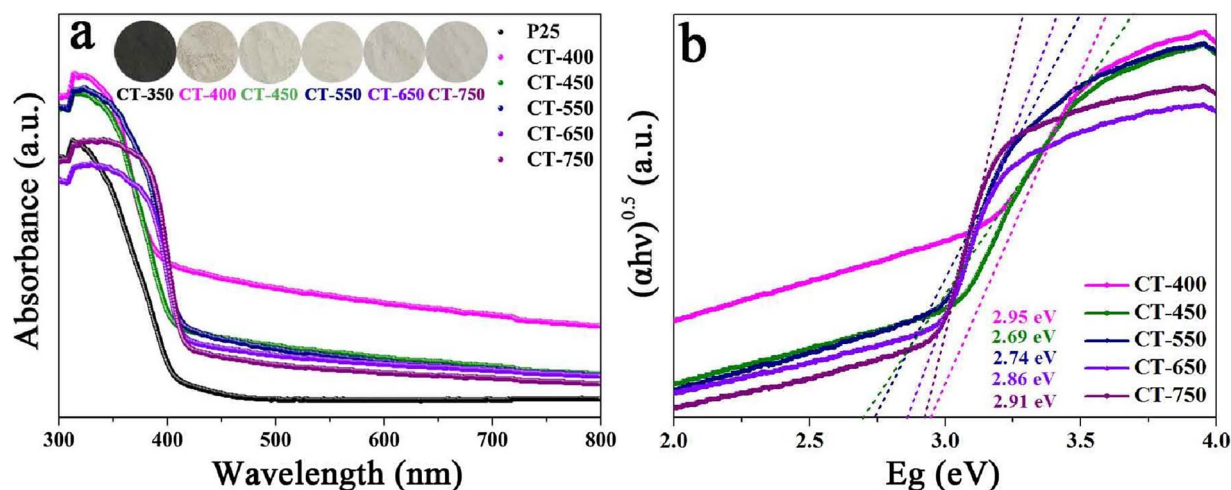
Fig. 7. (a) UV–vis diffuse reflectance spectra of P25 and CT samples. The inset is a digital photograph of CT samples. (b) Tauc plot for band gap determination of CT samples.

450 from 360 nm to 410 nm, which is ascribed to the large number of defects in CT-550, CT-650 and CT-750 [33].

Theoretical calculation is a perfect method to simulate the specific microstructure, and provides in-depth insight to the electronic properties of the nanomaterials, making us understand the experimental phenomena better [34]. Herein, we use the models of TiO_2 and its carbonate-doped counterpart (Fig. S16) to study the band gap and electronic properties. Density functional theory (DFT) calculations were carried out to study the effect of carbonate doping on the electronic structure of TiO_2. As shown in Fig. S16, the structure of carbonate-doped TiO_2 has four C–O bonds which are formed by connecting one carbon dopant with three lattice oxygen atoms. Then, we used GGA + U to optimize the structures for both TiO_2 (Fig. S17) and carbonate-doped TiO_2 (Fig. 8a and c), and calculate the density of states (DOS). Compared to the DOS of undoped anatase and rutile TiO_2, the carbonate-doping produces band tail states near the conduction and valence band

edges of anatase and rutile TiO_2, thus decreases the bandgap by 0.8 and 0.6 eV, respectively. And the calculation results are consistent with the Tauc plot (Fig. 7b). The decrease in the bandgap of the carbonate-doped TiO_2 can extent the light adsorption from ultraviolet to visible light region. To further give a visual image about the chemical bonds due to carbon doping, electron density maps are given as shown in Fig. 10b and d (3D maps in Fig. S18). The bond lengths of X-O in both anatase and rutile TiO_2 decreased after titanium substituted by carbon atoms. The electron difference density maps illustrate the mainly σ bonds are formed through combination of C 2p orbital and O sp hybrid orbital mainly located in deep valence region.

3.4. Charge-carrier separation and transfer

In order to explicitly demonstrate the functional role of a phase junction in charge separation, the PEC performances of CT samples
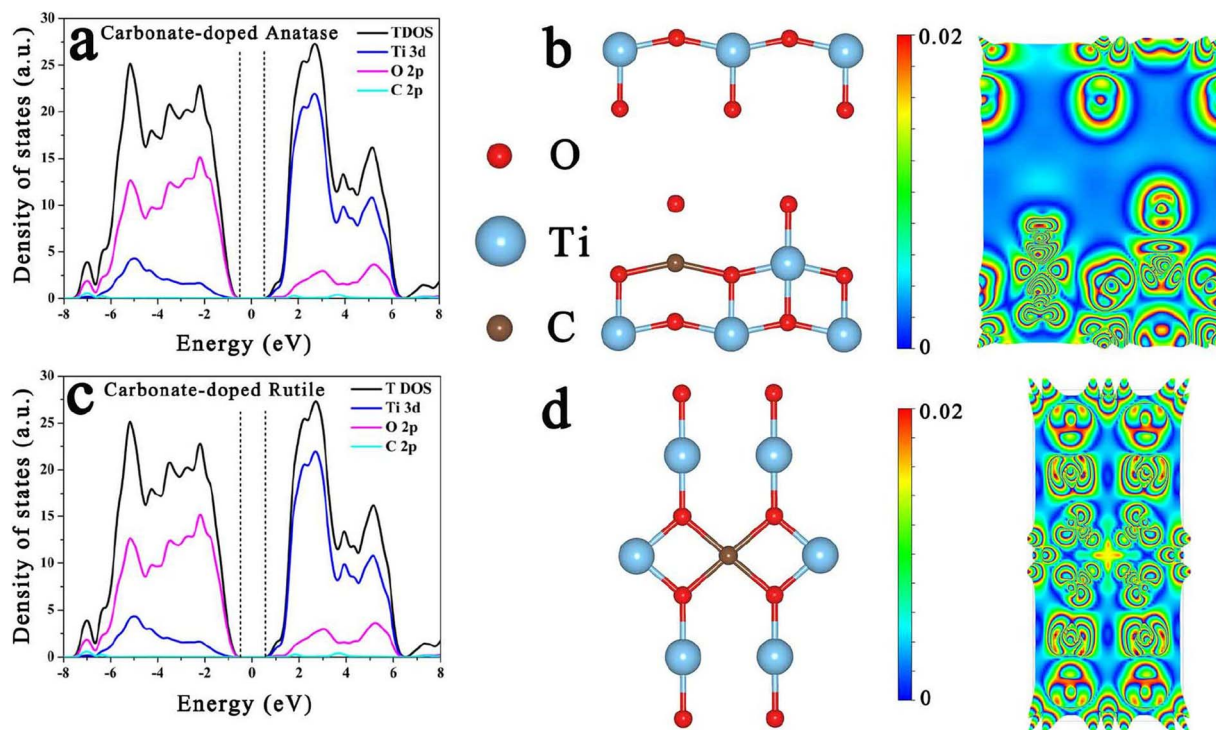

Fig. 8. Calculated density of states plot (a) and 2D structures (b) of carbonate-doped anatase and rutile TiO_2 cleaved along (2 0 0) and (−1 1 0), respectively, and corresponding electron difference density maps.
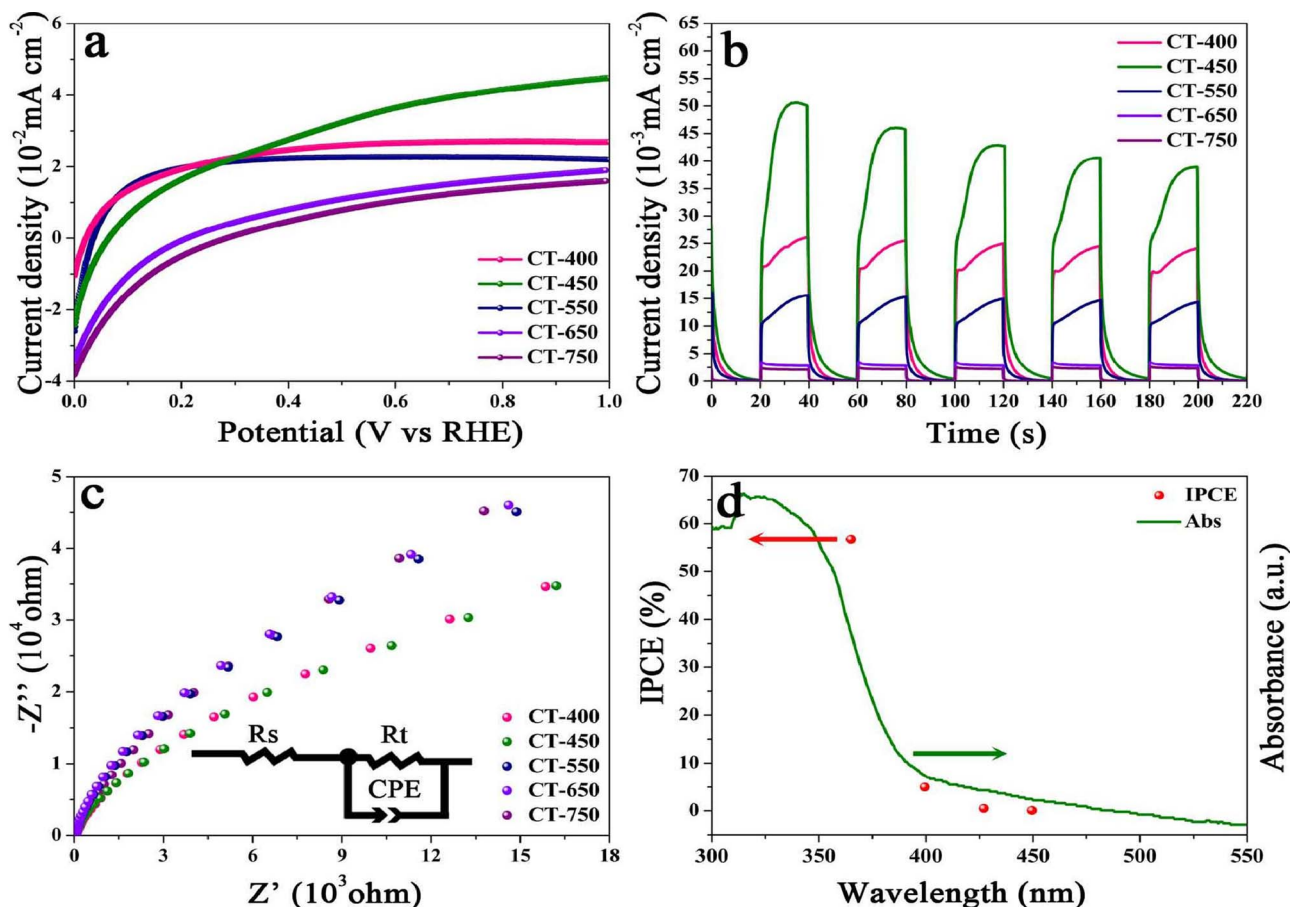
Fig. 9. PEC performances and characterizations of different CT samples: (a) J-V curves of different CT samples under 300 W Xenon lamp illumination (scan rate, 5 mv s^{-1}). (b) Transient photocurrent curves of different CT samples. (c) Electrochemical impedance spectra and (d) Ultraviolet-visible absorbance spectrum and IPCE of CT-450 sample.
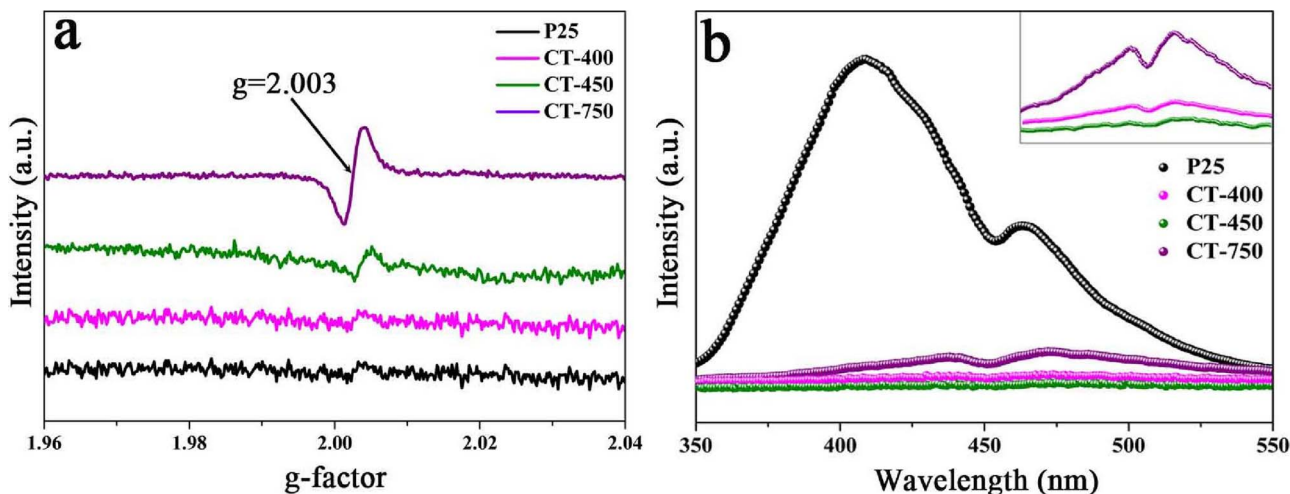

Fig. 10. Room-temperature EPR (a) and PL (b) spectra of P25, CT-400, CT-450 and CT-750.

were investigated by measuring the photocurrent densities under 300 W Xenon lamp and incident photon-to-current efficiency (IPCE) in a three-electrode electrochemical system. Fig. 9a shows the J-V curves of the CT samples. And the CT-450 sample exhibits a photocurrent density of ca. 0.045 mA cm^{-2} at 1.0 VRHE, which is about 1.5 and 2 times higher than those obtained for the CT-400 and CT-750 samples, respectively. The improved PEC performance of CT-450 verifies the importance of phase alignment for achieving efficient charge separation and collection in a PEC system[35]. However, the CT-400 sample exhibits a higher photocurrent density than that of CT-550, which has an anatase/ rutile phase alignment of 44:56. And this is attributed to the more carbon species in CT-400 and it is well known that graphitic carbon is a high work function material with excellent electron-accepting and transport properties [22]. And the optimization of carbon species and phase junction make CT-450 have the highest PEC performance. Furthermore, the notable improvement in separation and transport efficiency of the excited electron-hole pairs for CT-450 was further confirmed by the transient photocurrent response experiments as shown in Fig. 9b. When the light was successively switched on and off, a series of almost identical signals were obtained for all the CT samples, which can

also be observed from the J-V curves in Fig. S19. However, the photocurrent density of CT-450 sample, 0.045 mA cm^{-2}, is about 2 and 18 times higher than that of CT-400 and CT-750 samples, respectively, implying that CT-450 significantly enhanced the electron mobility by reducing the recombination of electron-hole pairs. Fig. 9c displays the EIS Nyquist plots of the CT samples. In fact, the EIS Nyquist plots can be well simulated to the equivalent electrical circuit as shown in Fig. 9c inset, in which Rs and Rt are the electrolyte solution resistance and the interfacial charge-transfer resistance/electrolyte, respectively [36]. Among all the samples, CT-450 shows the smallest diameter, suggesting its lowest resistance for interfacial charge transfer from electrode to electrolyte molecules. Therefore, combined with the above analysis, it is deemed that CT-450 possesses the strongest capability to not only separate photo-generated electron-hole pairs, but also transfer them to the reactant molecules adsorbed on the surface-active sites, implying its outstanding competence as a high-performance photocatalyst. As seen with the CT-450 sample, an appreciable IPCE appears when wavenumber is less 420 nm, indicating that the enhanced photocatalytic activities are more strongly related to the improved photo-excited e$^-$/h$^+$ separation efficiency than the broad visible light absorption (Fig. 9d). Therefore, the anatase/rutile phase junction and carbon doping have great effect on the charge separation and transfer, which inhibit the electron-hole pair recombination, and leading to efficient photocatalytic water splitting activity.

EPR (electron paramagnetic resonance) and PL (photoluminescence) spectra were used to further investigate the charge carrier trapping, migration and transfer in the samples. Herein, EPR spectra were used to explore the generation of oxygen vacancy in the samples. As shown in Fig. 10a, P25 and CT-400 samples have hardly any paramagnetic signal, whereas the CT-450 and CT-750 samples show an obvious EPR signal at g = 2.003, which can be assigned to the paramagnetic oxygen vacancy [37]. In addition, the EPR intensity of CT-750 is stronger than CT-450, which corresponds to the increase in the content of oxygen vacancies, and this is in accordance with the XPS analysis. It is accepted that the oxygen vacancies can capture and bind the electrons so that the paramagnetic resonance is generated, and oxygen vacancies are very important defects in TiO$_2$, which largely affect the chemical and physical properties of TiO$_2$ [37]. Furthermore, the PL spectra, which come from the recombination of free carriers, were used to understand the fate of electron-hole pairs. As can be seen from Fig. 10b, CT-400, CT-450 and TT-750 samples show much lower intensity than P25, indicating the recombination of electron-hole pairs has been effectively inhibited. And the inset shows the enlarge of the PL spectra of CT samples, CT-400 and CT-450 show lower PL intensity, which is resulted from the more carbon species that can effectively enhance the migration of electrons and suppress the electron-hole recombination [3]. Meanwhile, the lowest PL intensity of CT-450 can be abstracted to the synergistic effect of the anatase-rutile mixed phases, which have a positive role in the separation of electron-hole pairs. And for CT-750, the more oxygen vacancies make the average distance the electrons can move shorter, which make the oxygen vacancies bind easily electrons to form excitons. Therefore, the separation of electron-hole pairs in CT-450 are easier, which can effectively improve the photocatalytic activity.

3.5. Photocatalytic performance and the mechanism

The photocatalytic activity of CT samples was evaluated by hydrogen production from water under simulated solar light using Pt as cocatalyst and triethanolamine as hole scavenger. As shown in Fig. 11a, a peak hydrogen evolution rate of 4734.9 μmol h^{-1} g^{-1} is achieved at the calcination temperature is 400 °C (CT-400), which is nearly five times higher than that of CT-750. This is because that anatase TiO$_2$ exhibits a higher photocatalytic activity compared with rutile TiO$_2$, and the carbon species in CT-400 efficiently enhance charges separation. Once hole-electron are generated, electrons will be attracted

immediately to the carbon layers due to electrostatic force and rapidly pass through them to reach the active reaction sites. Further increasing the temperature to 450 °C, a highest hydrogen evolution rate (ca. 6108 μmol h^{-1} g^{-1}) was obtained by CT-450, which is higher than most values reported for C-doping TiO$_2$ photocatalysts and one dimensional TiO$_2$ photocatalysts (Table S2). The better photocatalytic performance of CT-450 than CT-400 can be attributed to the mixed phases in which the interface heterojunction between anatase and rutile phases can accelerate the separation of charge carriers and improve the transfer rate of photo-generated electrons and holes to carbon species. However, CT-550 and CT-650 show lower photocatalytic hydrogen evolution rate than CT-400 and CT-650, which also obtain two phases. This is ascribed to their limited light absorption, low surface area and poor charge transport capability. We then measured the apparent quantum efficiency on CT-450 at different light wavelengths by using various band-pass filters in the same reaction system. The AQE has been considered as an alternative indicator to appropriately assess the photocatalyst performance, and it is generally thought that the larger the AQE, the more efficient separation of photoinduced charge pair is, as well the photoactivity [22]. The trend in apparent quantum efficiency closely followed that of the absorbance measured by ultraviolet-visible spectroscopy (Fig. 11b), revealing bandgap-transtion-dependent hydrogen evolution behavior [38]. Notably, a high apparent quantum efficiency of about 83% was obtained at 365 nm. Considering the transmittance of quartz glass, that is, around 95%, the internal quantum efficiency is estimated to be approaching 90%. In other words, 90% of the photons excite electron/hole pairs can convert them into hydrogen atoms. However, the AQE at 420, 475 and 520 nm are only 3.86%, 0.62% and 0.063%, respectively, resulting from the lower light absorption. Furthermore, the stability of the photocatalyst is critical for its practical application. In order to evaluate the stability of CT-450, the photocatalytic reaction system was purged every five hours for 30 min to remove the hydrogen inside. It can be observed from Fig. 11c that the photocatalytic activity does not show significant deterioration over four consecutive recycling experiments, indicating the robustness of CT-450.

On basis of the above results, the photocatalytic hydrogen evolution mechanism of mesoporous carbonate-doped phase-junction TiO$_2$ nanotubes can be proposed. The previous researches show that four successive steps are included in the photocatalytic reaction: (a) incident light absorption; (b) electron-hole pairs production; (c) electron-hole pairs separation and migration; (d) photocatalyst surface redox reaction [36]. Since the four steps are intimately associated with the inherent feature of a photocatalyst, including morphology, electronic, crystal and textural structures, a comprehensive effect of all the features would enable a synergetic impact of the four steps, thus the photocatalytic activity can be promoted significantly [39]. CT-450 prepared in this work can be regarded as a convincing example. Firstly, both the porous and electronic structure of CT-450 have the ability to harvest more light. One the one hand, the porous structure of CT-450 can increase the optical path by multiple reflection effect, thus enhancing light harvesting. As can be seen from Fig. 12, the incident light can be trapped by the porous structure, some photons can be absorbed directly, while some photons are reflected within the porous structure until completely absorbed. On the other hand, the band gaps of both anatase and rutile TiO$_2$ have been narrowed by the carbonate species (Fig. 7a). More light harvesting is the premise of the high photocatalytic activity. Secondly, electron-hole pairs separation and migration and graphite carbon species are simultaneously tuned to optimize the separation and transfer of photo-generated electron-hole pairs. The intimate homo-junctions between anatase and rutile phases should be very favorable for the transfer of the charge carriers within the hybrids and thus improve the separation of electron-hole pairs. This band structure can significantly facilitate the smooth flow of photo-generated conduction electrons from anatase to rutile and valance holes from rutile to anatase, respectively [18]. Moreover, we have also noted that the graphite carbon species are mostly deposited on the surface of TiO$_2$, which have excellent electron-
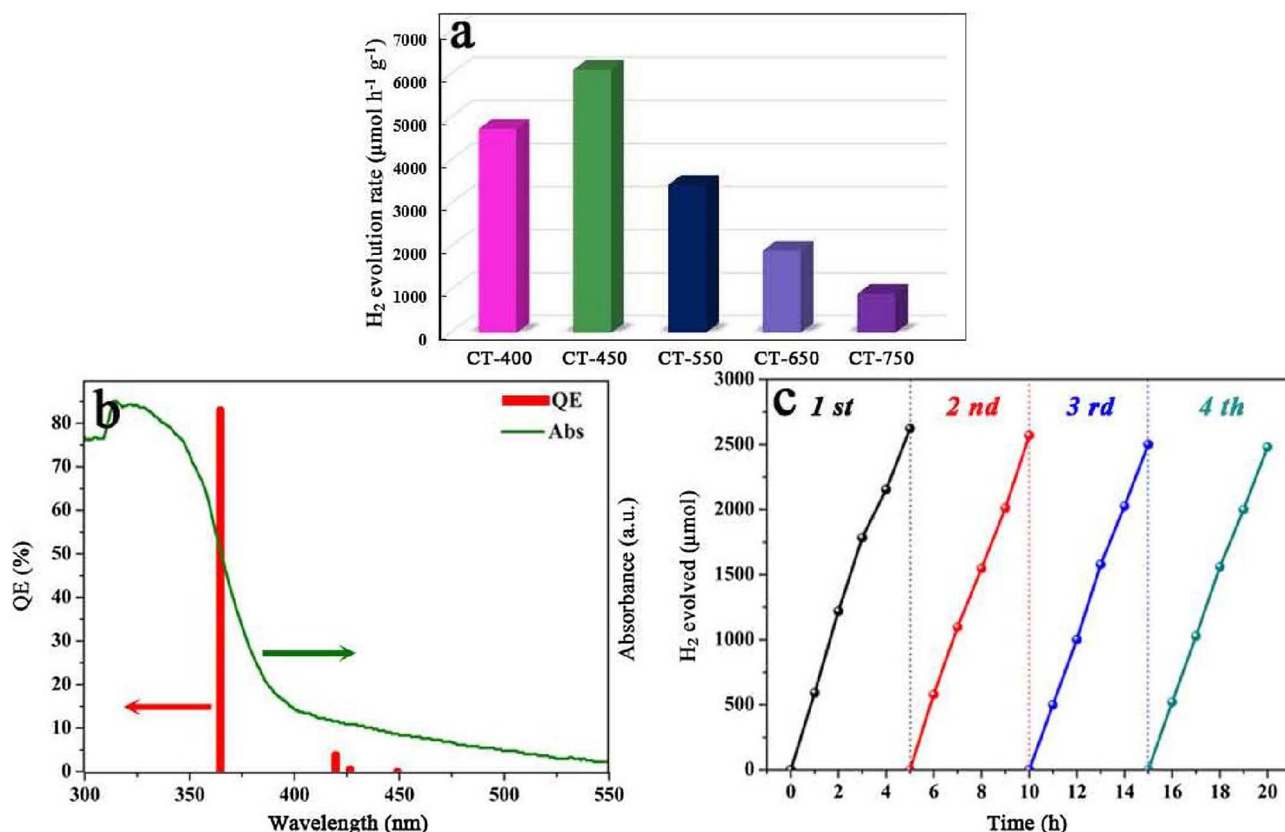
Fig. 11. (a) Photocatalytic H_2 evolution rate for CT samples under simulated solar light. (b) QE of CT-450 at 365, 420, 475 and 520 nm. (c) Cycling test of photocatalytic H_2 evolution over CT-450.

accepting and transport properties. Thus the electrons will be attracted immediately to graphite carbon by electrostatic force and rapidly pass through them to reach the active reaction sites. Improving the separation of photoinduced electron and hole pairs is main reason behind the high photocatalytic activity. Finally, the surface structures are tailored to supply more surface area for active sites, as well as facilitate the transfer of reactants and products through the porous structures. In the process of photocatalytic water splitting, the protons/TEOA molecules in the solution can easily reach the adsorption centers on the surface of CT-450, then the adsorbed protons/TEOA molecules can react with the interfacial electron/hole. At last, proton/TEOA molecules undergo surface redox reactions in the catalytic centers, producing H_2/oxidative products. Therefore, the excellent strategy involves morphology, electronic, crystal and textural structures can optimize the four successive steps in photocatalytic H_2 production, and a significant synergetic effect

in the photocatalytic activity is achieved.

4. Conclusions

In summary, we have demonstrated a novel and general approach, namely, olive oil-assisted electrospinning, for synthesizing mesoporous carbonate-doped phase-junction TiO_2 nanotubes with a combination of features attractive for photocatalytic hydrogen evolution. These features include well-defined morphology, high light absorption, tunable electronic, crystal and textural structures. The new photocatalyst exhibits enhanced visible light absorption, enlarged surface area, improved charge mobility and accelerated charge-to-surface migration, due to its carbon-doped system and porous nanotube architecture. Thus, a very high photocatalytic hydrogen evolution activity of $6108\,\mu mol\,h^{-1}\,g^{-1}$ was achieved. Notably, the theoretical and
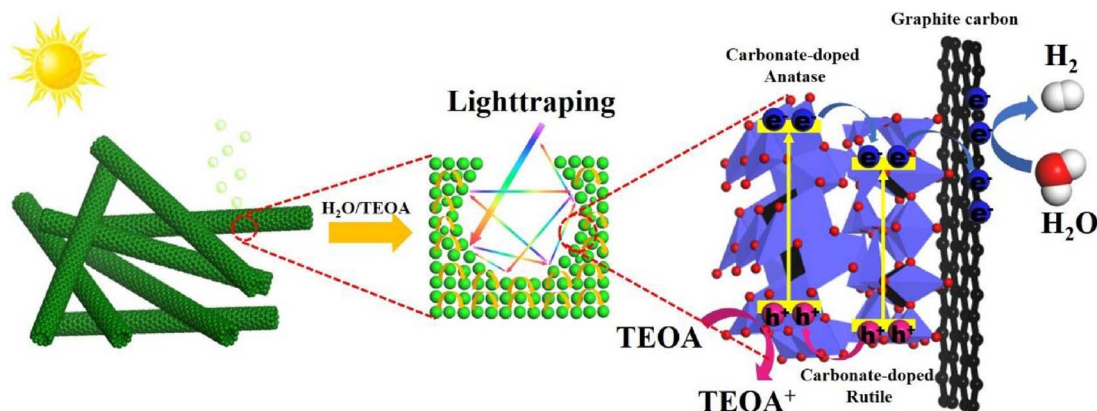

Fig. 12. Photocatalytic hydrogen evolution mechanism of mesoporous carbonate-doped phase-junction TiO_2 nanotubes.

experimental studies reveal that carbonate could be incorporated into the TiO_2 lattice and the TiO_2 bandgap could be narrowed to significantly improve the visible light photocatalytic hydrogen evolution. Moreover, the intimate homo-junctions between anatase and rutile phases and the graphite carbon on the surface of TiO_2 can significantly help promote the separation of charge carriers. This work highlights that an easy and general strategy can be used to prepare a high efficiency porous TiO_2 nanotubes photocatalyst, which can provide new insights for preparing new TiO_2-based photocatalysts without any complex and expensive modification.

Acknowledgments

Appendix A. Supplementary data

Supplementary data associated with this article can be found, in the online version, at https://doi.org/10.1016/j.apcatb.2017.11.069.

References

[1] J. Li, G. Zhan, Y. Yu, L. Zhang, Nat. Commun. 7 (2016) 11480.
[2] L. Jing, J. Zhou, J.R. Durrant, J. Tang, D. Liu, H. Fu, Energy Environ. Sci. 5 (2012) 6552–6558.
[3] J. Liu, L. Han, N. An, L. Xing, H. Ma, L. Cheng, J. Yang, Q. Zhang, Appl. Catal. 202 (2017) 642–652.
[4] J. Schneider, M. Matsuoka, M. Takeuchi, J.L. Zhang, Y. Horiuchi, M. Anpo, D.W. Bahnemann, Chem. Rev. 114 (2014) 9919–9986.
[5] B. Liu, L.M. Liu, X.F. Lang, H.Y. Wang, X.W. Lou, E.S. Aydil, Energy Environ. Sci. 7 (2014) 2592–2597.
[6] H.L. Hou, L. Wang, F.M. Gao, G.D. Wei, B. Tang, W.Y. Yang, T. Wu, J. Am. Chem. Soc. 136 (2014) 16716–16719.
[7] Y.G. Yang, M. Suzuki, H. Fukui, H. Shirai, K. Hanabusa, Chem. Mater. 18 (2006) 1324–1329.
[8] Z.L. Yang, Z.W. Niu, X.Y. Cao, Z.Z. Yang, Y.F. Lu, Z.B. Hu, C.C. Han, Angew. Chem., Int. Ed. 42 (2003) 4201–4203.
[9] J.F. Wang, J.P. Zhang, B.Y. Asoo, G.D. Stucky, J. Am. Chem. Soc. 125 (2003) 13966–13967.
[10] Z.P. Yao, F.Z. Jia, S.J. Tian, C.X. Li, Z.H. Jiang, X.F. Bai, ACS Appl. Mater. Interfaces 2 (2010) 2617–2622.
[11] M. Xu, P.M. Da, H.Y. Wu, D.Y. Zhao, G.F. Zheng, Nano Lett. 12 (2012) 1503–1508.
[12] Y.C. Wang, Y.Y. Zhang, J. Tang, H.Y. Wu, M. Xu, Z. Peng, X.G. Gong, G.F. Zheng, ACS Nano 7 (2013) 9375–9383.
[13] S. In, A. Orlov, R. Berg, F. Garcia, S. Pedrosa-Jimenez, M.S. Tikhov, D.S. Wright, R.M. Lambert, J. Am. Chem. Soc. 129 (2007) 13790–13791.
[14] R. Asahi, T. Morikawa, T. Ohwaki, K. Aoki, Y. Taga, Science 293 (2001) 269–271.
[15] R. Asahi, T. Morikawa, T. Ohwaki, K. Aoki, Y. Taga, Science 295 (2002) 627.
[16] S. Wang, W.C. Li, L. Zhang, Z.Y. Jin, A.H. Lu, J. Mater. Chem. A 2 (2014) 4406–4412.
[17] T. Ohno, T. Tsubota, K. Nishijima, Z. Miyamoto, Chem. Lett. 33 (2004) 750–751.
[18] Y. Zhou, C.H. Chen, N.N. Wang, Y.Y. Li, H.M. Ding, J. Phys. Chem. C 120 (2016) 6116–6124.
[19] G.G. Liu, G.X. Zhao, W. Zhou, Y.Y. Liu, H. Pang, H.B. Zhang, D. Hao, X.G. Meng, P. Li, T. Kako, J.H. Ye, Adv. Funct. Mater. 26 (2016) 6822–6829.
[20] S. Na Phattalung, S. Limpijumnong, J. Yu, Appl. Catal. B 200 (2017) 1–9.
[21] B.A. Lu, C.Q. Zhu, Z.X. Zhang, W. Lan, E.Q. Xie, J. Mater. Chem. 22 (2012) 1375–1379.
[22] C.X. Zhao, H. Luo, F. Chen, P. Zhang, L.H. Yi, K.Y. You, Energy Environ. Sci. 7 (2014) 1700–1707.
[23] H.B. Wu, H.H. Hng, X.W. Lou, Adv. Mater. 24 (2012) 2567–2571.
[24] S. Chuangchote, J. Jitputti, T. Sagawa, S. Yoshikawa, ACS Appl. Mater. Interfaces 1 (2009) 1140–1143.
[25] J. Wu, Environ. Sci. Technol. 41 (2007) 1723–1728.
[26] S.S. Lee, H.W. Bai, Z.Y. Liu, D.D. Sun, Appl. Catal. B 140 (2013) 68–81.
[27] C. Bueno-Ferrer, S. Parres-Esclapez, D. Lozano-Castelló, A. Bueno-López, J. Rare Earths 28 (2010) 647–653.
[28] J.M. Liu, Q.C. Zhang, J.C. Yang, H.Y. Ma, M.O. Tade, S.B. Wang, J. Liu, Chem. Commun. 50 (2014) 13971–13974.
[29] D.E. Gu, Y. Lu, B.C. Yang, Y.D. Hu, Chem. Commun. (2008) 2453–2455.
[30] C.W. Lai, S. Sreekantan, P. San E, W. Krengvirat, Electrochim. Acta 77 (2012) 128–136.
[31] A. Sinhamahapatra, J.-P. Jeon, J.-S. Yu, Energy Environ. Sci. 8 (2015) 3539–3544.
[32] H. Wang, X. Qiu, W. Liu, D. Yang, Appl. Surf. Sci. 426 (2017) 206–216.
[33] F.N. Sayed, O.D. Jayakumar, R. Sasikala, R.M. Kadam, S.R. Bharadwaj, L. Kienle, U. Schurmann, S. Kaps, R. Adelung, J.P. Mittal, A.K. Tyagi, J. Phys. Chem. C 116 (2012) 12462–12467.
[34] G. Xie, K. Zhang, B. Guo, Q. Liu, L. Fang, J.R. Gong, Adv. Mater. 25 (2013) 3820–3839.
[35] A. Li, Z. Wang, H. Yin, S. Wang, P. Yan, B. Huang, X. Wang, R. Li, X. Zong, H. Han, C. Li, Chem. Sci. 7 (2016) 6076–6082.
[36] J. Ran, T.Y. Ma, G. Gao, X.-W. Du, S.Z. Qiao, Energy Environ. Sci. 8 (2015) 3708–3717.
[37] X.Y. Pan, M.Q. Yang, X.Z. Fu, N. Zhang, Y.J. Xu, Nanoscale 5 (2013) 3601–3614.
[38] H. Kaga, A. Kudo, J. Catal. 310 (2014) 31–36.
[39] S. Liu, J. Xia, J. Yu, ACS Appl. Mater. Interfaces 7 (2015) 8166–8175.